

# Multiphoton nonlinear frequency mixing effects on the coherent electromagnetically induced absorption spectra of $^{85}\text{Rb}$ atoms under a longitudinal magnetic field: Theory and experiment

Zeeshan Ali Safdar Jadoon <sup>1</sup>, Heung-Ryoul Noh <sup>2,\*</sup> and Jin-Tae Kim <sup>1,†</sup>

<sup>1</sup>Department of Photonic Engineering, Chosun University, Gwangju 61452, Korea

<sup>2</sup>Department of Physics, Chonnam National University, Gwangju 61186, Korea



(Received 26 July 2020; accepted 4 December 2020; published 22 December 2020)

Multiphoton nonlinear frequency mixing effects on coherent electromagnetically induced absorption spectra of  $^{85}\text{Rb}$  atoms using two orthogonal linear polarizations of strong-coupling and weak probe beams are investigated theoretically and experimentally with respect to an applied longitudinal magnetic field and coupling powers. Herein, we confirm that at least five-photon interactions in solving density matrix equations for the  $F_g = 3 \rightarrow F_e = 4$  transition of  $^{85}\text{Rb}$  atoms are required to explain experimentally observed coherent electromagnetically induced absorption spectra when a quantum axis is selected as the propagation direction of co-propagating coupling and probe laser beams. Distinct calculated spectral differences owing to variations in the magnetic field and coupling power between three- and five-photon interactions are confirmed. The obtained asymmetrical spectral shapes match very well with those calculated from five-photon interactions considering the off-resonant  $F_g = 3 \rightarrow F_e = 2, 3$  transitions. Genuine coherent spectral shapes are observed with a single laser combined with two acousto-optic modulators, wherein the spectral resolution is limited because of the decoherence rate between Zeeman sublevels in the ground state from transit-time relaxation.

DOI: [10.1103/PhysRevA.102.063714](https://doi.org/10.1103/PhysRevA.102.063714)

## I. INTRODUCTION

Multiphoton nonlinear frequency mixing effects [1–19] between coupling and probe laser beams are crucial in calculating accurate coherent spectral shapes in coupling-probe spectroscopy in a degenerate two-level system (DTLS) [6–19] utilizing optical density matrix elements. Each optical density matrix element can be expanded by Fourier series taken to all orders in the case of strong coupling and probe beams [18,19]. Different oscillating frequencies of the coupling and probe beams resulting from multiphoton interactions greater than three-photon interactions (3PIs) for multiphoton coherence oscillations between the magnetic sublevels in strong coupling and probe beams should be considered for all possible contributions to probe absorption to investigate precise coherent spectral profiles. However, the Rabi frequency of the probe beam is treated to first order in the case of the weak probe beam [6–17].

Coherent spectra from coupling-probe spectroscopy up to 3PIs have been investigated extensively. Ultranarrow anti-holes in coupling-probe spectroscopy are explained through inelastic collisions and 3PIs in simple two-level systems with reservoir states such as hyperfine or Zeeman sublevels [4]. Henceforth, the transfer of coherence and population from electromagnetically induced absorption (EIA) in a DTLS with 3PIs has been investigated theoretically [7,8]. The propagation equations in Ref. [12] included Floquet expansion to all orders ( $n$ ) given by Eq. (10) in Ref. [12]; however, they determined the propagation equations utilizing 3PIs with  $n_{\max} = 2$ .

Akulshin *et al.* [17] reported ultranarrow coupling-probe coherent spectra using a single laser with two acousto-optic modulators (AOMs) without theoretical analysis. Subsequently, dependencies of coupling-probe power, optical field polarization, and magnetic field on coupling-probe coherent spectra in DTLSs were investigated using only 3PIs [6] to clarify the observed spectra in Ref. [17].

Selecting the appropriate quantum axis [3,13,18,20] as the polarization direction of the coupling or probe beam, or in the case of weak-coupling beams, 3PIs can be applied to solve optical Bloch equations (OBEs). Chen *et al.* [3] demonstrated the advantages of selecting the appropriate quantum axis such that complex calculations can be avoided and experimental spectra with 3PIs can be interpreted intuitively in a coupling-probe experiment involving a degenerate three-level system without an external magnetic field. Ultranarrow observed EIA spectral features owing to population and coherence transfer for the same and orthogonal linear polarization configurations were investigated through 3PIs [9] without phenomenological constants and an external magnetic field with the appropriate quantum axis as the polarization direction of the coupling beam.

In the case of strong coupling and probe beams few works have been reported considering multiphoton interactions greater than 3PIs. The authors in Refs. [18,19] considered higher-order photon interactions given by  $a_{1,\max} = F_g + F_e$  in Zeeman coherences with a single frequency in Table I in Ref. [18] for different transitions of magnetic sublevels between a strong  $\sigma^+$ -polarized control beam and a probe beam with either  $\sigma^-$  or  $\pi$  polarization with comparable intensity to the coupling beam. However, they could not see higher-order nonlinear frequency mixing effects such as five-photon interactions (5PIs) with only a single oscillating frequency at

\*hrnoh@chonnam.ac.kr

†kimjt@chosun.ac.kr

higher coupling-probe intensities because both the coupling and probe beams act on different hyperfine transitions instead of same hyperfine transitions like our case. Equations (4)–(8) governing OBEs in strong coupling and probe beams in Ref. [19] follow a similar mathematical formulation as Eqs. (12)–(16) representing OBEs in Ref. [18] so that Ref. [19] falls into a similar category as Ref. [18].

External magnetic fields in addition to coupling-probe spectra with strong coupling power in DTLSSs render the calculation of coupling-probe coherent spectra with more than 3PIs even more complicated. Selecting the quantum axis as the direction of an external longitudinal magnetic field (LMF) is convenient to simplify the system for solving OBEs. The applied magnetic fields can be both transverse and longitudinal simultaneously [5,20,21], only transverse [22–25], or only longitudinal [1,12,15,26,27] to the propagation direction of the co-propagating coupling and probe lasers.

Margalit *et al.* [5] theoretically investigated the effect of transverse magnetic fields in the degenerate three-level system. They obtained the same results even after setting the quantization axis as an arbitrary direction via 3PI in OBEs as adopted in their reference (Ref. [15]). The authors in Ref. [15] could not realize the higher-order multiphoton frequency mixing effects due to 5PIs, but realized 3PI effects for the transfer of coherence in EIA.

We have calculated coherent absorption spectral profiles considering different oscillating frequencies of the coupling and probe beams resulting from two different cutoff photon interactions such as 3PIs [9], and 5PIs with or without LMF. When selecting the propagation direction of co-propagating coupling and probe laser beams as a quantum axis acting on the same transitions of magnetic sublevels between strong-coupling and weak probe frequencies, at least 5PIs described in detail in the theoretical section should be considered, unlike selecting the polarization direction of a coupling beam as a quantum axis, to match the experimentally observed EIA spectra with or without LMF. Distinct spectral differences between 3PIs and 5PIs calculated in the case of acting on the same transitions of magnetic sublevels rather than different transitions of magnetic sublevels between strong coupling and probe frequencies have been unraveled using the coupling-probe experimental coherent spectra in DTLSS.

We also realize that off-resonant transitions ( $F_g = 3 \rightarrow F_e = 2$  and  $F_e = 3$ ) near the resonant  $F_g = 3 \rightarrow F_e = 4$  transition contribute to the asymmetry of the observed spectra. At large magnetic fields or weak coupling powers, 5PI calculations are similar to 3PI calculations, which also match well with the experimentally observed spectra.

The experiment is performed with a single laser combined with two AOMs to achieve the mutual coherence of the coupling-probe fields, wherein the linewidth is limited owing to the decoherence rate between Zeeman sublevels in the ground state from the transit-time relaxation.

## II. THEORY FOR 3PIS AND 5PIS IN DTLSS UNDER LMF

The energy-level diagram for the  $5S_{1/2}(F_g = 3) \rightarrow 5P_{3/2}(F_e = 4)$  transition of  $^{85}\text{Rb}$  atoms is shown in Fig. 1(a). The co-propagating coupling and probe beams are linearly polarized in directions perpendicular to each

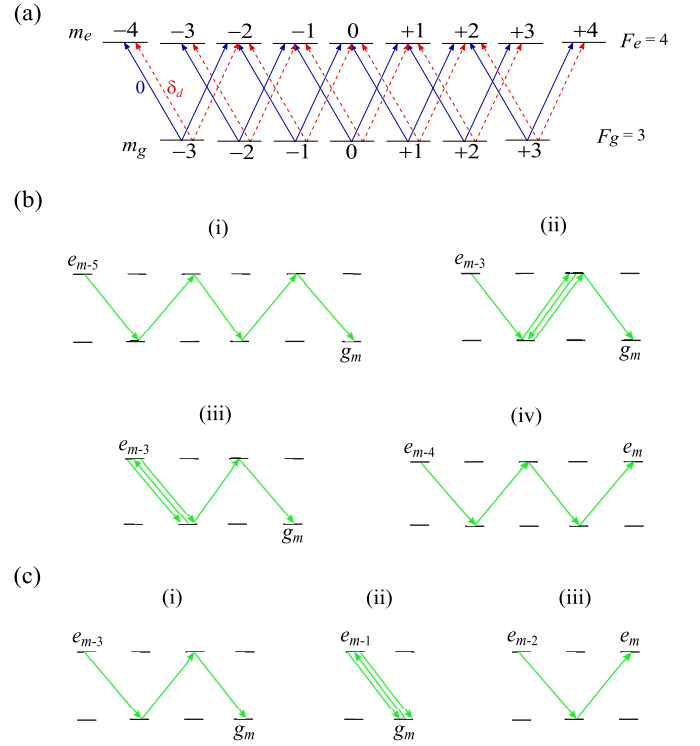


FIG. 1. (a) Transition schemes with two circularly polarized coupling and probe beams for energy level of the  $5S_{1/2}(F_g = 3) \rightarrow 5P_{3/2}(F_e = 4)$  transition of  $^{85}\text{Rb}$  atoms. Typical possible routes connecting the states by coupling and probe photons are 5PIs (b-i) between  $|e_{m-5}\rangle$  and  $|g_m\rangle$ , (b-ii) between  $|e_{m-3}\rangle$  and  $|g_m\rangle$ , (b-iii) between  $|e_{m-3}\rangle$  and  $|g_m\rangle$ , and (b-iv) between  $|e_{m-4}\rangle$  and  $|e_m\rangle$ , and 3PIs (c-i) between  $|e_{m-3}\rangle$  and  $|g_m\rangle$ , (c-ii) between  $|e_{m-1}\rangle$  and  $|g_m\rangle$ , and (c-iii) between  $|e_{m-2}\rangle$  and  $|e_m\rangle$ . The green arrows denote the transitions by the mixed coupling and probe beams simultaneously to avoid confusion.

other. The detuning of the probe (coupling) beam in the rest frame of an atom moving with velocity  $v$  is expressed as  $\delta_1 = \delta_p - kv$  ( $\delta_2 = \delta_c - kv$ ), where  $\delta_p$  ( $\delta_c$ ) is the detuning of the probe (coupling) beam, and  $k$  ( $= 2\pi/\lambda$ ) and  $\lambda$  are the wavevector and wavelength of the laser beams, respectively. To implement an applied magnetic field in the calculation, we select the propagation direction of the laser beams as a quantization axis. The density matrix equation in the rotating frame of frequency of the coupling beam is expressed as

$$\dot{\rho} = -\frac{i}{\hbar}[H_0 + V, \rho] + \dot{\rho}_{\text{sp}}, \quad (1)$$

where  $\rho$  is the density operator. The atomic Hamiltonian  $H_0$  is expressed as

$$H_0 = \sum_{m=-4}^4 \hbar(-\delta_2 + g_e \mu_B B m) |F_e = 4, m\rangle \langle F_e = 4, m| + \sum_{m=-3}^3 \hbar g_g \mu_B B m |F_g = 3, m\rangle \langle F_g = 3, m|, \quad (2)$$

where  $\mu_B$  is the Bohr magneton,  $B$  is the LMF, and  $g_e$  ( $= 1/2$ ) and  $g_g$  ( $= 1/3$ ) are the Landé  $g$  factors of the states  $5P_{3/2}(F_e = 4)$  and  $5S_{1/2}(F_g = 3)$ , respectively. In Eq. (1), the interaction

Hamiltonian  $V$  is expressed as

$$V = \sum_{q=\pm 1} \sum_{m=-3}^3 \frac{\hbar}{2} (a_q e^{-i\delta_d t} \Omega_1 + b_q \Omega_2) C_m^{m+q} \times |F_e = 4, m+q\rangle \langle F_g = 3, m| + \text{H.c.}, \quad (3)$$

where  $\Omega_1$  ( $\Omega_2$ ) and  $a_{\pm} = \mp 1/\sqrt{2}$  ( $b_{\pm} = i/\sqrt{2}$ ) are the Rabi frequency and the coefficient of the electric field of the probe (coupling) beam in the spherical bases, respectively. In Eq. (3), H.c. denotes the Hermitian conjugate,  $C_{m_g}^{m_e}$  is the normalized transition strength between the states  $|F_e = 4, m_e\rangle$  and  $|F_g = 3, m_g\rangle$  [2], and  $\delta_d (\equiv \delta_1 - \delta_2 = \delta_p - \delta_c)$  is the difference in the detunings of the probe and coupling beams. Thus, “0” (“ $\delta_d$ ”) in Fig. 1(a) denotes the relative detuning of the coupling (probe) beam with respect to the frequency of the coupling beam. In Eq. (1),  $\dot{\rho}_{\text{sp}}$  represents the spontaneous emission term, whose matrix elements are shown in Eq. (3) in Ref. [13]. The finite interaction time between atoms and laser beams is considered in the calculation by employing a transit relaxation constant [14].

Because two different frequencies of the electric fields appear simultaneously for the available transitions, as shown in Fig. 1(a), the density matrix elements can be decomposed into many Fourier components. In the 5PI (3PI) calculation, the 5PI (3PI) for the optical coherences and four-photon (two-photon) interactions for the populations and Zeeman coherences are considered. Hence, in the 5PI calculation, the density matrix elements of the optical coherence, Zeeman coherences, and populations are explicitly expressed as

$$\begin{aligned} \rho_{e_{m\pm\epsilon}, g_m} &= \rho_{e_{m\pm\epsilon}, g_m}^{(1)} + \rho_{e_{m\pm\epsilon}, g_m}^{(2)} e^{-i\delta_d t} + \rho_{e_{m\pm\epsilon}, g_m}^{(3)} e^{i\delta_d t} \\ &\quad + \rho_{e_{m\pm\epsilon}, g_m}^{(4)} e^{-2i\delta_d t} + \rho_{e_{m\pm\epsilon}, g_m}^{(5)} e^{2i\delta_d t} + \rho_{e_{m\pm\epsilon}, g_m}^{(6)} e^{-3i\delta_d t}, \\ \rho_{e_{m\pm\mu}, e_m} &= \rho_{e_{m\pm\mu}, e_m}^{(1)} + \rho_{e_{m\pm\mu}, e_m}^{(2)} e^{-i\delta_d t} + \rho_{e_{m\pm\mu}, e_m}^{(3)} e^{i\delta_d t} \\ &\quad + \rho_{e_{m\pm\mu}, e_m}^{(4)} e^{-2i\delta_d t} + \rho_{e_{m\pm\mu}, e_m}^{(5)} e^{2i\delta_d t}, \\ \rho_{g_{m\pm\nu}, g_m} &= \rho_{g_{m\pm\nu}, g_m}^{(1)} + \rho_{g_{m\pm\nu}, g_m}^{(2)} e^{-i\delta_d t} + \rho_{g_{m\pm\nu}, g_m}^{(3)} e^{i\delta_d t} \\ &\quad + \rho_{g_{m\pm\nu}, g_m}^{(4)} e^{-2i\delta_d t} + \rho_{g_{m\pm\nu}, g_m}^{(5)} e^{2i\delta_d t}, \\ \rho_{\alpha, \beta} &= \rho_{\beta, \alpha}^* \end{aligned} \quad (4)$$

where  $\epsilon = 1, 3$ , and  $5$ ;  $\mu = 0, 2$ , and  $4$ , and  $\nu = 0, 2$ , and  $4$ , for all the relevant values of  $m$ . We use the simplified notations for the matrix elements in Eq. (4), as follows:

$$\begin{aligned} \rho_{e_{m'}, g_m} &= \langle F_e = 4, m' | \rho | F_g = 3, m \rangle, \\ \rho_{e_{m'}, e_m} &= \langle F_e = 4, m' | \rho | F_e = 4, m \rangle, \\ \rho_{g_{m'}, g_m} &= \langle F_g = 3, m' | \rho | F_g = 3, m \rangle. \end{aligned} \quad (5)$$

Notably, the elements  $\rho_{e_{m\pm 1}, g_m}^{(2)}$  in Eq. (4) contribute to the probe absorption. This is because the matrix elements of  $\rho_{e_{m\pm 1}, g_m}^{(2)} e^{-i\delta_d t}$  contribute to the dipole moment oscillating at the frequency of the probe field and are responsible for the probe absorption as in Eq. (7) below.

Figure 1(b) shows typical connection configurations among various possible configurations for 5PIs between the magnetic sublevels of the excited and ground states by the coupling and probe photons. Figure 1(b-i) shows the 5PI between the sublevels  $|e_{m-5}\rangle$  and  $|g_m\rangle$ . In each emission

(absorption) process, the contribution to the net oscillation frequencies are given by  $\{0, -\delta_d\}$  ( $\{0, \delta_d\}$ ). Therefore, the resultant oscillation frequencies via the 5PI in Fig. 1(b-i) are given by

$$\begin{aligned} &\{0, -\delta_d\} \oplus \{0, \delta_d\} \oplus \{0, -\delta_d\} \oplus \{0, \delta_d\} \oplus \{0, -\delta_d\} \\ &\rightarrow \{0, -\delta_d, \delta_d, -2\delta_d, 2\delta_d, -3\delta_d\}. \end{aligned}$$

Figures 1(b-ii) and 1(b-iii) show two typical 5PIs between the sublevels  $|e_{m-3}\rangle$  and  $|g_m\rangle$ . The resultant oscillation frequencies for these connections are the same as those for the connection between the sublevels  $|e_{m-5}\rangle$  and  $|g_m\rangle$ . Although there exist other connections between the sublevels  $|e_{m-3}\rangle$  and  $|g_m\rangle$ , the oscillation frequencies remain unchanged. Therefore, we can conclude that the oscillation frequencies for the optical coherences  $\rho_{e_{m\pm\epsilon}, g_m}$  within the 5PIs are given by  $\{0, -\delta_d, \delta_d, -2\delta_d, 2\delta_d, -3\delta_d\}$ . Figure 1(b-iv) shows the four-photon interactions between the sublevels  $|e_{m-4}\rangle$  and  $|e_m\rangle$ , and the oscillation frequencies are given by

$$\begin{aligned} &\{0, -\delta_d\} \oplus \{0, \delta_d\} \oplus \{0, -\delta_d\} \oplus \{0, \delta_d\} \\ &\rightarrow \{0, -\delta_d, \delta_d, -2\delta_d, 2\delta_d\}. \end{aligned}$$

In an analogous method, we can construct the decompositions of the other density matrix elements in Eq. (4). Because we can select nonzero components of the density matrix elements, the OBEs in Eq. (1) can be solved numerically in a rapid and efficient way. In this sense, we can state that our method of solving OBEs is distinct from the perturbative approach as discussed in Ref. [28], where how subsequent orders of  $\rho$  are coupled and the density matrix  $\rho$  to a given order  $\rho^{(n)}$  can thus be expressed in terms of the elements  $\rho^{(n-1)}$  of the next-lowest order to solve the OBEs.

In the 3PI calculation, the optical and Zeeman coherences (and populations) in Eq. (4) are truncated at  $\rho^{(4)}$  and  $\rho^{(3)}$ , respectively, and are explicitly expressed as

$$\begin{aligned} \rho_{e_{m\pm\epsilon}, g_m} &= \rho_{e_{m\pm\epsilon}, g_m}^{(1)} + \rho_{e_{m\pm\epsilon}, g_m}^{(2)} e^{-i\delta_d t} + \rho_{e_{m\pm\epsilon}, g_m}^{(3)} e^{i\delta_d t} \\ &\quad + \rho_{e_{m\pm\epsilon}, g_m}^{(4)} e^{-2i\delta_d t}, \\ \rho_{e_{m\pm\mu}, e_m} &= \rho_{e_{m\pm\mu}, e_m}^{(1)} + \rho_{e_{m\pm\mu}, e_m}^{(2)} e^{-i\delta_d t} + \rho_{e_{m\pm\mu}, e_m}^{(3)} e^{i\delta_d t}, \\ \rho_{g_{m\pm\nu}, g_m} &= \rho_{g_{m\pm\nu}, g_m}^{(1)} + \rho_{g_{m\pm\nu}, g_m}^{(2)} e^{-i\delta_d t} + \rho_{g_{m\pm\nu}, g_m}^{(3)} e^{i\delta_d t}, \end{aligned} \quad (6)$$

where  $\epsilon = 1, 3$ , and  $5$ ;  $\mu = 0, 2$ , and  $4$ ; and  $\nu = 0, 2$ , and  $4$ . Figure 1(c) shows how typical oscillation frequencies for 3PIs are generated. In an analogous method for 5PIs, the resultant oscillation frequencies via the 3PI for the optical coherence with  $\Delta m = 3$  ( $\Delta m = 1$ ) in Fig. 1(c-i) [Fig. 1(c-ii)] are given by  $\{0, -\delta_d\} \oplus \{0, \delta_d\} \oplus \{0, -\delta_d\} \rightarrow \{0, -\delta_d, \delta_d, -2\delta_d\}$ . In Fig. 1(c-iii), the frequencies of the Zeeman coherence are given by  $\{0, -\delta_d\} \oplus \{0, \delta_d\} \rightarrow \{0, -\delta_d, \delta_d\}$ . Comparing Eqs. (4) and (6), The terms of  $\rho_{e_{m\pm\epsilon}, g_m}^{(5)}$  and  $\rho_{e_{m\pm\epsilon}, g_m}^{(6)}$  neglected in the 3PI calculation are considered in the 5PI calculation. This kind of inclusion of more terms for the density matrix elements increases the precision of the calculation.

After inserting Eqs. (2)–(4) into Eq. (1), we obtain coupled differential equations for the matrix elements, which are then solved numerically as functions of  $\delta_p$ ,  $\delta_c$ , and  $\nu$ . Finally, the

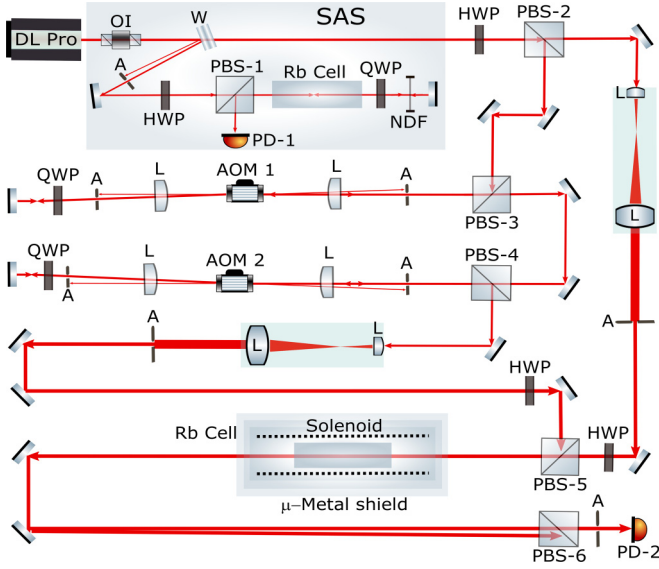


FIG. 2. Schematic experimental setup using a single laser combined with two AOMs. Component symbols: OI, optical isolator; W, window; SAS, saturation absorption spectroscopy; HWP, half-wave plate; PBS, polarizing beam splitter; A, aperture, QWP, quarter-wave plate; NDF, neutral density filter; L, lens; PD, photodiode; AOM, acousto-optic modulator.

absorption coefficient of the probe beam is expressed as

$$\alpha = -\frac{3\lambda^2 N_{\text{at}}}{2\pi \Omega_1} \int_{-\infty}^{\infty} \frac{dv}{\sqrt{\pi}u} e^{-(v/u)^2} \times \text{Im} \left[ \sum_{q=\pm 1} \sum_{m=-3}^3 a_q^* C_m^{m+q} \rho_{e_{m+q}, g_m}^{(2)} \right], \quad (7)$$

where  $N_{\text{at}}$  is the atomic vapor density in the cell, and  $u$  is the most probable speed in the cell.

Here, we describe the effect of the quantization axis on the accuracy of the calculation. When the direction of the coupling field is selected as the quantization axis, only the optical coherences  $\rho_{e_m, g_m}$  between the sublevels with  $\Delta m = 0$  do not vanish and all the other optical coherences vanish. Thus, when the probe field is very weak, because the optical coherences with  $\Delta m \neq 0$  are not significant, the calculation can be very accurate although only 3PI processes are considered.

However, when the direction of the laser field is selected as the quantization axis, all the optical coherences with  $\Delta m = \pm 1, \pm 3, \pm 5, \dots$  do not vanish. Therefore, higher photon interactions are required to obtain a sufficient accuracy in the calculation such as 5PI processes. Because it is convenient to select the direction of the magnetic field as the quantization axis in the presence of a longitudinal magnetic field, at least 5PI calculation is needed to obtain accurate calculated results of the EIA spectra.

### III. EXPERIMENTAL PROCEDURE

The schematic of the experimental setup is shown in Fig. 2. A laser beam for the  $5S_{1/2} \rightarrow 5P_{3/2}$  transition of  $^{85}\text{Rb}$  atoms at 780 nm is generated using a tunable external cavity diode laser [29] with a typical output power of 100 mW in a single-

mode regime. A window (W) is used to extract 4% of the total output power of the laser beam for a frequency locking to the  $F_g = 3 \rightarrow F_e = 4$  resonance line of  $^{85}\text{Rb}$  atoms for saturated absorption spectroscopy. The polarizing beam splitter 1 (PBS-1) passes a strong  $p$ -polarized coupling beam and reflects a weak counterpropagating  $s$ -polarized probe beam reflected through a neutral density filter (NDF) from a mirror into photodiode 1 (PD-1) to detect the saturated absorption signals. A quarter-wave plate (QWP) is utilized to change the incoming  $p$ -polarized coupling beam to an  $s$ -polarized probe beam. The NDF controls the power ratio between the coupling and probe beams.

EIA spectra are obtained using a single laser beam combined with two AOMs with a central frequency of 80 MHz in a double-pass scheme, as shown in Fig. 2. The strong main beam transmitting the W is separated into a weak  $p$ -polarized probe beam directed to a half-wave plate (HWP) in front of PBS-5 and a strong  $s$ -polarized coupling beam directed to AOM-1 using PBS-2 and an HWP after the W. The coupling beam transmits AOM-1 and a QWP positioned behind AOM-1 and then reflects it back to AOM-1 through the QWP from a mirror. The reflected coupling beam transmits PBS-3, and the procedure performed in AOM-1 is similarly implemented in AOM-2. Subsequently, the coupling beam from AOM-2 is expanded by  $5\times$  to combine at PBS-2 with the weak probe beam expanded after PBS-2 to obtain a uniform intensity across a 4-mm-diam beam. Hence, AOM-1 in the double-pass configuration upshifts the frequency ( $f$ ) of the initially  $s$ -polarized coupling beam by +160 MHz and passes through PBS-3, whereas when scanning AOM-2, the laser beam is downshifted to the original frequency by  $-160$  MHz with the scanning detuning of  $2\Delta$  owing to the double-pass configuration. PBS-5 is used to overlap the co-propagating probe and coupling beams with the orthogonal-linear polarizations upon a vapor cell containing  $^{85}\text{Rb}$  atoms at room temperature.

An external LMF is applied to the vapor cell with a solenoid surrounding the vapor cell shielded with five layers of  $\mu$ -metal sheets to remove the effect of stray and earth's magnetic fields inside the cell. Probe absorption is detected at the PD-2 when PBS-6 is used to separate the  $s$ -polarized coupling beam, and an intersection angle of  $\sim 0.1$  mrad is maintained for possible leakage due to polarization rotations introduced by the applied external magnetic field.

### IV. RESULTS AND DISCUSSIONS

In this section, a comparison of the observed coherent spectra with the calculated spectra is presented to elucidate the observed coherent spectral characteristics from 5PIs, discernible from those of 3PIs with respect to the coupling powers and LMF.

#### A. Spectral features depending on coupling powers without LMF

Dependencies of coupling powers on the EIA spectra with a weak linearly polarized probe beam perpendicular to the coupling beam resonant with the  $F_g = 3 \rightarrow F_e = 4$  transition of  $^{85}\text{Rb}$  atoms at room temperature without a magnetic field (i.e.,  $B = 0$ ) are investigated. Numerical spectral calculations

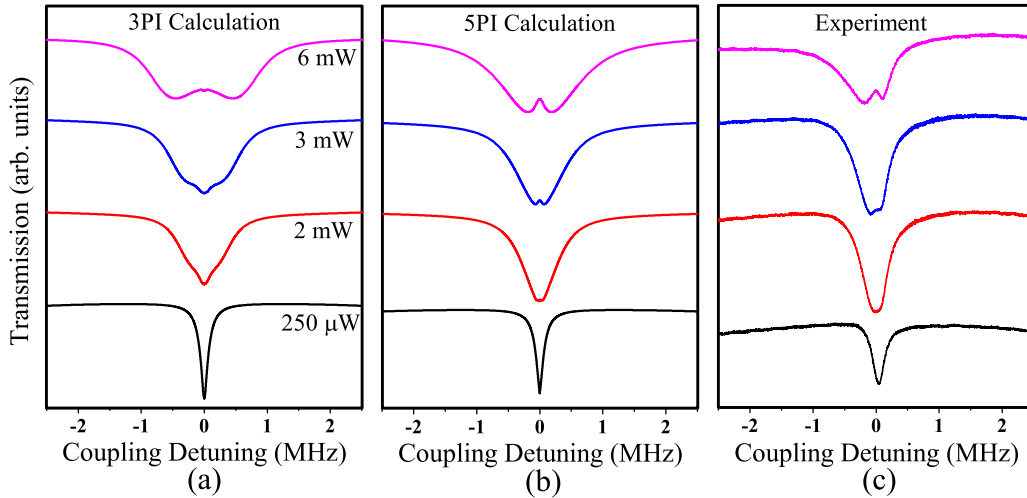


FIG. 3. EIA spectra without magnetic field by varying coupling power (250  $\mu$ W to 6 mW) with fixing probe power at 15  $\mu$ W. Calculation using (a) 3PI, (b) 5PI, and (c) experimental measurements.

utilizing the 3PI and 5PI as well as experimentally measured EIA spectra by varying the coupling field powers (0.25 to 6 mW) with a fixed probe of 15  $\mu$ W and a laser beam diameter of 4 mm are shown in Fig. 3.

The spectral calculations utilizing the 3PI and 5PI are shown in Figs. 3(a) and 3(b), respectively, and the experimental measurement in Fig. 3(c) shows a similar spectral feature as those from 3PI and 5PI in the weak coupling power of 0.25 mW. For strong coupling powers above 2 mW, discernible spectral feature differences are observed in the central region of the spectra between the 3PI and 5PI. The 3PI calculation is characterized by an ultranarrow dip embedded in a narrow dip at the central region. The amplitude of the ultranarrow dip decreases with the increase in the coupling power, and the sign of the dip inverts after  $\sim 4$  mW [not shown in Fig. 3(a)]. With the increase in the coupling power, the narrow dip splits into two broad dip features, as shown in the coupling power of 6 mW. The central EIA signal for atoms moving at a constant velocity become split due to Autler-Towns splitting (ATS) from the strong coupling power. After performing an average over Maxwell-Boltzmann velocity distribution in the calculation, two separated EIA signals as shown in Fig. 3(b) are created, and therefore a central EIT-like transmission peak emerges [9]. However, ATS owing to the ultranarrow dip feature at the center of the spectra in the lower coupling powers. Broad ATS features beside the central ultranarrow dip are resolved with the linewidth of 479 kHz at 5 mW [not shown in Fig. 3(a)] and 480 kHz at 6 mW, as shown in Fig. 3(a).

However, the 5PI calculation is characterized by a narrow and ultranarrow peak embedded in a narrow dip owing to ATS at the central region developing from 2.5 up to 6 mW with respect to the power increase, unlike the 3PI calculation. Broad ATS features beside the central ultranarrow peak further develop in the separations with linewidths of 62 and 147 kHz at 3 and 6 mW of coupling powers, respectively, as shown in Fig. 3(b), whereas such ATS is not observed at lower powers.

The experimental coherent spectra show that ATS develops weakly at the central region at 2.5 mW, but increases with the

coupling power up to 6 mW, similar to the 5PI calculation. The amplitudes of the broad ATS feature beside the central ultranarrow and asymmetric peak further develop in the separations with linewidths of 83 and 178 kHz at 3 and 6 mW of coupling powers, respectively, as shown in Fig. 3(c). The experimentally observed spectra show spectral behaviors similar to those from the 5PI calculation, as shown in Fig. 3(b), with ATS at higher powers. The asymmetric spectra are due to the off-resonant  $F_g = 3 \rightarrow F_e = 2$  and  $F_g = 3 \rightarrow F_e = 3$  transitions of  $^{85}\text{Rb}$  atoms. The detailed explanations for the origin of the asymmetric spectra are given in Sec. IV E.

From these analyses, 5PI calculations instead of 3PI calculations at higher coupling powers provide reliable results for predicting experimental EIA spectra with the quantum axis as the propagation direction of laser fields without a magnetic field. It should be noted that the coherence between the magnetic sublevels connected via coupling and probe beams increases when the laser beam's intensities are weak. As the laser beam's intensities increase, the coherence reaches a maximum when the effective Rabi frequency is comparable to the linewidth of the transition under consideration, and then decreases [30].

### B. Spectral features depending on coupling powers with LMF of 0.3 G

A static magnetic field is applied in the direction of laser propagations in the coupling-probe system such that in the spectral simulation, a quantum axis can be selected as the direction of the applied LMF to simplify the system for solving OBEs.

Unlike the case without an applied magnetic field, the spectra split into two Zeeman sidebands beside the central spectrum. The splittings of the sidebands owing to the Zeeman effect match well with the observed ones, which can be used as frequency calibration. Unlike the case without an applied magnetic field described in Sec. IV A, spectral mixing effects are observed on the coherent spectra owing to Zeeman splitting and ATS due to strong coupling powers. Hence, the calculated and observed spectral features exhibit ATS even at

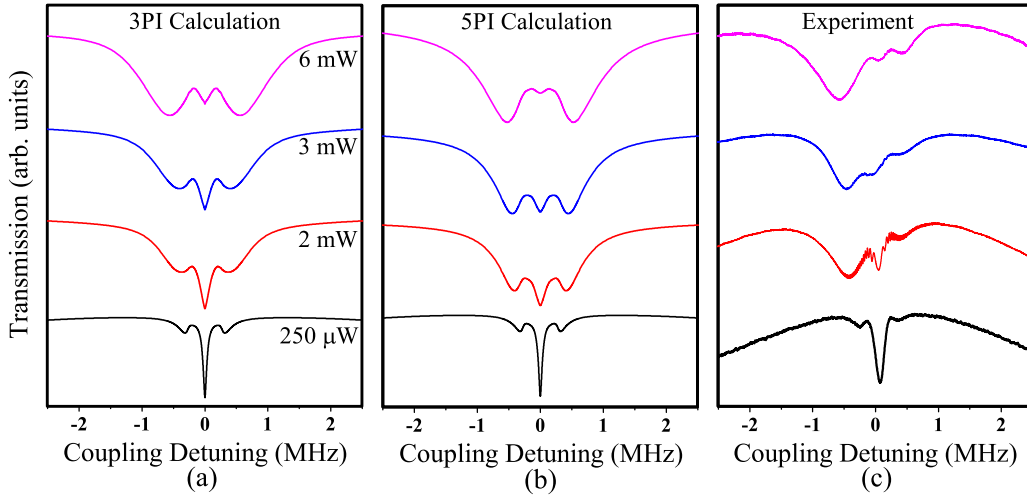


FIG. 4. EIA spectra with 0.3 G magnetic field by varying coupling power (250  $\mu\text{W}$  to 6 mW) and fixing probe power at 15  $\mu\text{W}$ . Calculation using (a) 3PI, (b) 5PI, and (c) experimental measurements.

lower powers, unlike the spectra without an applied field. At higher coupling powers, the spectra due to the ATS effect mix more significantly with the spectra from the Zeeman effect. Spectral differences between the 3PI and 5PI results from the central part of the spectra are shown in Figs. 4(a) and 4(b).

Numerical spectral calculations utilizing the 3PI and 5PI are shown in Figs. 4(a) and 4(b), respectively, and the experimental measurement in Fig. 4(c) shows a similar spectral feature in the weak coupling power of 0.25 mW. In the calculated EIA spectra utilizing the 3PI, the amplitude of the ultranarrow dip at the central region of the spectra decreases slowly compared with the amplitude of the ultranarrow dip obtained from the 5PI with the increases in the coupling powers. The spectral profiles of the 3PI calculation differ from those of the 5PI calculation. The linewidth is 147 kHz at 3 mW and increases to 153 kHz at 6 mW of coupling power, as shown in Fig. 4(a). The amplitudes of the dips decrease with the increases in the coupling power up to 6 mW. In the calculated EIA spectra utilizing the 5PI, the linewidths are 157 and 143 kHz at 3 and 6 mW of coupling powers, respectively, as shown in Fig. 4(b).

Figure 4(c) shows the experimentally measured EIA spectra by varying the coupling field powers (0.25 to 6 mW) with a fixed probe of 15  $\mu\text{W}$  and an applied LMF of 0.3 G. Because of the applied LMF, the spectral feature with the increased linewidth of EIA spectra owing to ATS and the magnetic field differs significantly from that with the linewidths in the case without an LMF. The spectral asymmetry of the observed spectra is larger than that without a magnetic field; this is attributable to the off-resonant transitions of  $^{85}\text{Rb}$  atoms (see the explanations in Sec. IV E below). The linewidths are 192 and 174 kHz at 3 and 6 mW, respectively, comparable to the calculated linewidths utilizing the 5PI. Evidently, the 5PI calculation instead of the 3PI calculation provides better matches with the observed spectra.

### C. Spectral features depending on coupling powers with LMF of 1 G

At a higher magnetic field of 1 G as shown in Fig. 5, the 3PI [Fig. 5(a)] and 5PI [Fig. 5(b)] calculations differ less

for each power, although the central amplitudes between the 3PI and 5PI indicate slight differences at higher powers, as discussed in Sec. IV B. For other weaker magnetic field cases, the central peaks of the 5PI are smaller than those of the 3PI. However, the decrease in the amplitude of the central peak with respect to the increase in the coupling power is slower than the decrease in the amplitude in lower magnetic fields. The slight differences between the 3PI and 5PI calculations at a higher magnetic field may result from the large Zeeman shifts of the energies of the degenerate sublevels. In this case, each transition shown in Fig. 1(a) becomes nonresonant, and diminishes the coherent effects, and accordingly the effect of higher-photon interactions becomes insignificant.

The central EIA dip at  $B = 1$  G for the measured signal [Fig. 5(c)] with 250  $\mu\text{W}$  has a 162-kHz linewidth, whereas a narrow linewidth is obtained in the calculations, i.e., 51 and 55 kHz using the 3PI and 5PI, respectively. The separation of EIA sidebands is proportional to the applied magnetic field magnitude, i.e., approximately 1 MHz per 1 G. No major trend difference is observed between the measurements and calculations except the broad linewidth and lower amplitude of the observed experimental EIA signal. The broad linewidth of the experimental measurement is due to the sustained angle of 0.3 mrad between the probe and coupling fields to eliminate the coupling beam leakage on the detector, whereas a missing ultranarrow region below 80 kHz resulted in a lower amplitude of the measured EIA signal. The central EIA signals decrease with respect to the increases in the magnetic field, thereby reducing N-type connections between the magnetic sublevels owing to the Zeeman splittings.

### D. Spectral features depending on LMF with fixed coupling power of 3 mW

In this section, magnetic field dependencies on EIA spectra are investigated at an intermediate coupling power of 3 mW. Numerical spectral calculations utilizing the 3PI and 5PI as well as experimental measurements by varying the magnetic field (0 to 0.9 G) with a fixed probe (15  $\mu\text{W}$ ) and coupling power (3 mW) at the evident ATS limit of the coupling powers

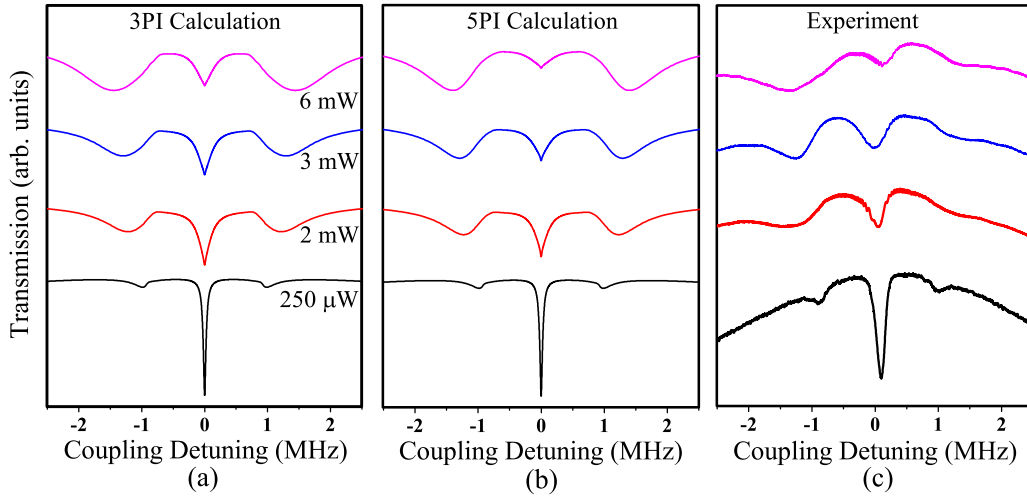


FIG. 5. EIA spectra with 1 G magnetic field by varying coupling intensity ( $250 \mu\text{W}$  to 6 mW) and fixing probe at  $15 \mu\text{W}$ . Calculation using (a) 3PI, (b) 5PI, and (c) experimental measurements.

are shown in Figs. 6(a), 6(b) and 6(c), respectively. An applied magnetic field separates the EIA lines owing to the Zeeman effect, as shown in Fig. 6; consequently, distinct spectral differences owing to the magnetic field and ATS due to strong coupling powers between the 3PI and 5PI calculations in the central region of the spectra are observed. Hence, spectral features owing to multiphoton frequency mixing effects are discernible through spectral comparisons between the calculated and observed spectra.

Major spectral trend differences in the central region of the spectra from utilizing the 3PI and 5PI calculations are evident at lower magnetic fields, as discussed in Secs. IV B and IV C.

Unlike the case without an applied magnetic field described in Sec. IV A, spectral mixing effects are observed on the coherent spectra owing to the Zeeman splittings and ATS due to the strong coupling power. At higher coupling powers and the ATS limit, the spectra owing to the ATS effect are mixed with the spectra from the Zeeman effect. Spectral differences between the 3PI and 5PI resulting from the central part of the spectra are shown in Figs. 6(a) and 6(b). At lower magnetic fields of  $B = 0, 0.1, \text{ and } 0.3 \text{ G}$ , the spectral differences are evident because the ultranarrow signals at the central portion of the spectra have opposite signs with dips and peaks owing to coherent effects between the 3PI and 5PI, respectively. EIA

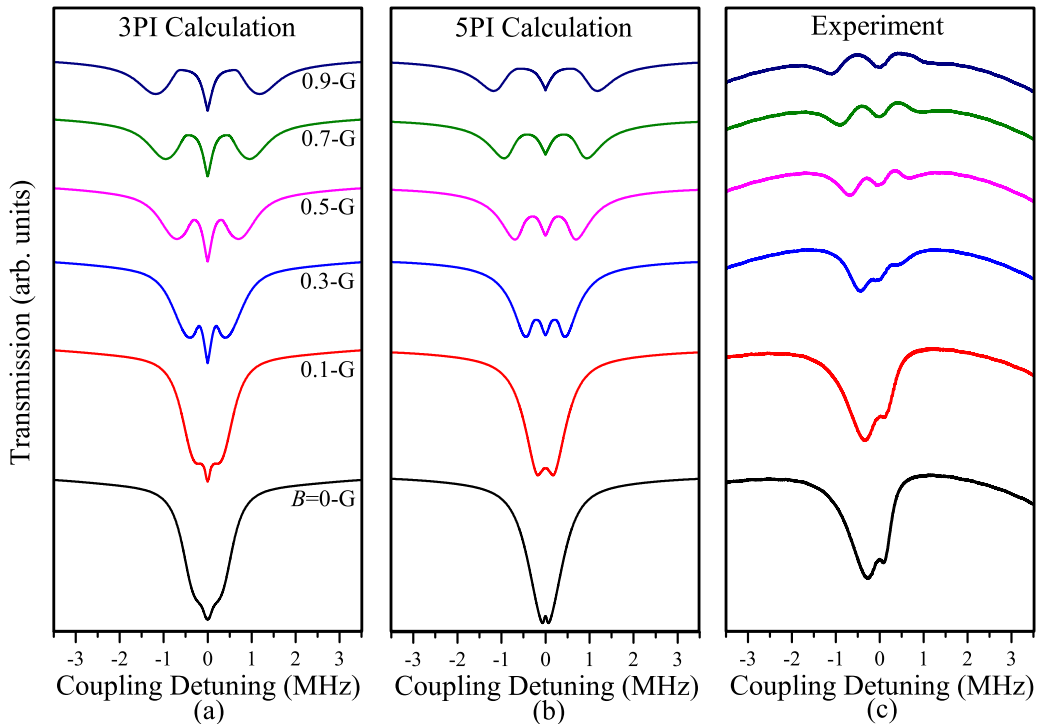


FIG. 6. EIA spectra by varying magnetic field (0 to 1 G) with fixed probe and coupling power of  $15 \mu\text{W}$  and 3 mW, respectively. Calculation using (a) 3PI, (b) 5PI, and (c) experimental measurements.

spectral energy separations from the Zeeman effect owing to magnetic fields of 0.1 to 0.9 G are larger than those of ATS owing to the coupling power.

The spectral profiles from the 3PI calculation differ from those of the 5PI calculation with the increase in the magnetic field. In the calculated EIA spectra from the 3PI, the amplitudes of the ultranarrow central dip for the 3PI calculation increase and reach the maximum and then decrease with the increase in the magnetic field. The minimum of the central dip in the 3PI is deeper than those of the sidebands at lower magnetic fields.

The ultranarrow central peak for the 5PI calculation below 0.3 G increases in amplitude and changes to an ultranarrow central dip above 0.1 G. The amplitude of the dip reaches the maximum and then decreases with the increase in the magnetic field. A peak is observed instead of a dip below 0.3 G, and the minimum central dip above 0.1 G in the 5PI calculation is slightly smaller than those of the sidebands, unlike in the 3PI case.

The experimental results are more similar to those of the 5PI calculation than the 3PI calculation for points wherein the starting point of the central EIA dip is above 0.1 G and the linewidth and ending point of the central peak are below 0.3 G.

In addition, the minimum central dip in the observed case is shallower than those at the sidebands, similar to those of the 5PI calculation. As described earlier, the experimental spectra are similar to the spectra from the 5PI calculation. For the experimental spectra, the background signal at the right side is higher than that at the left side, resulting in an asymmetric signal.

### E. Physical nature of asymmetric spectral features

To study the origin of large asymmetric spectral features shown in Fig. 7 (curve i) with the probe power of  $15 \mu\text{W}$ , the coupling power of 6 mW, and  $B = 0.3 \text{ G}$ , two different calculations with the 5PI process have been done: The first case is the calculation as shown in Fig. 7 (curve ii) when the off-resonant  $F_g = 3 \rightarrow F_e = 2$  and  $F_g = 3 \rightarrow F_e = 3$  transitions are included as well as the resonant  $F_g = 3 \rightarrow F_e = 4$  transition described in detail above. The second case is the calculation as shown in Fig. 7 (curve iii) when a transverse magnetic field of 30 mG is included to investigate the effects on asymmetrical spectra of any stray transverse magnetic field when only the resonant  $F_g = 3 \rightarrow F_e = 4$  transition is considered.

From the asymmetric behavior of the result shown in Fig. 7 (curve ii) without the transverse magnetic field of 30 mG we can readily interpret that the asymmetric spectrum results from the off-resonant transitions because when the transverse magnetic field of 30 mG is included, the asymmetric spectrum is not produced as shown in Fig. 7 (curve iii). Therefore, we can conclude that the asymmetric spectral feature found in the experiment results mainly from the effect of the off-resonant transitions. The calculation described in this section is preliminarily only to investigate the origin of the experimentally observed asymmetric spectra. The detailed study on the effect of the nonresonant transitions on the EIA spectra will be reported in a separate publication.

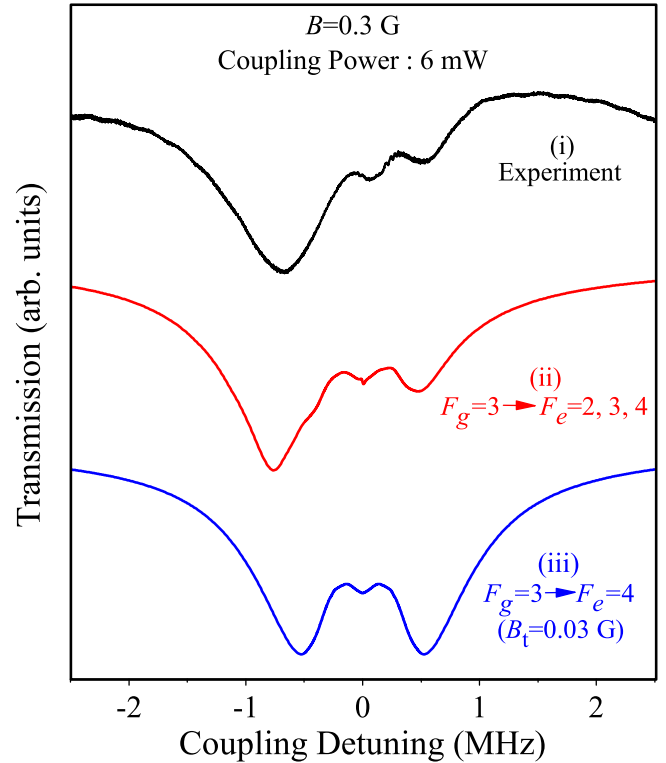


FIG. 7. EIA spectra with 0.3 G of magnetic field at coupling power of 6 mW and probe power of  $15 \mu\text{W}$  from (i) experimental measurement, (ii) calculation with considering the off-resonant  $F_g = 3 \rightarrow F_e = 2, 3$  transitions without the transverse magnetic field of 30 mG with 5PI, and (iii) calculation without considering the off-resonant  $F_g = 3 \rightarrow F_e = 2, 3$  transitions with the transverse magnetic field of 30 mG with 5PI.

### V. CONCLUSIONS

Multiphoton frequency mixing effects on coherent EIA spectra of  $^{85}\text{Rb}$  atoms are investigated theoretically and experimentally based on an applied LMF and coupling powers with two orthogonal linear polarizations of co-propagating strong coupling and weak probe beams. Coherent EIA spectra between 3PI and 5PI calculations owing to variations in the magnetic field magnitude and ATS due to strong coupling powers are distinguishable. The experiment is performed using a single laser combined with two AOMs to reveal the distinct coherent EIA spectra from the 5PI, wherein the linewidth is limited owing to the decoherence rate between Zeeman sublevels in the ground state from the transit-time relaxation.

We confirm that at least 5PIs are required for solving density matrix equations for the  $F_g = 3 \rightarrow F_e = 4$  transition of  $^{85}\text{Rb}$  atoms in the case where a quantum axis is selected as the propagation field direction to elucidate experimentally observed coherent EIA spectra from nonlinear multiphoton mixing effects.

We realize that the origin of observed asymmetrical spectra results mainly from off-resonant transitions ( $F_g = 3 \rightarrow F_e = 2, 3$ ) instead of a transverse stray magnetic field coming from an imperfect LMF. At large magnetic fields or weak coupling powers, 3PI calculations are sufficient to explain the observed coherent spectra with fewer pathways connected between the

sublevels. Although there are no significant differences between the experimental and calculated SPI results, the studies of the detailed effects of higher photon interactions exceeding SPI on the EIA spectra and more detailed analyses on origins of asymmetrical spectral behaviors must be pursued and are, in fact, currently in progress.

## ACKNOWLEDGMENTS

This work was supported by the National Research Foundation of Korea (NRF) grant funded by the Korea government (MSIT) (Grant No. 2020R1A2C1005499) and research fund from Chosun University (2016).

- [1] Y.-B. Dong, J.-R. Gao, and Dong Y.-E. Dong, Quantum coherent effects in multi-Zeeman-sublevel atomic systems, *Chin. Phys. B* **17**, 3306 (2008).
- [2] G. W. Choi and H.-R. Noh, Sub-Doppler DAVLL spectra of the D1 line of rubidium: A theoretical and experimental study, *J. Phys. B: At. Mol. Opt. Phys.* **48**, 115008 (2015).
- [3] Y. Chen, C. Lin, Y. Chen, and I. Yu, Quantization axes in coherent two-field spectroscopy, *J. Opt. Soc. Am. B* **19**, 1917 (2002).
- [4] D. Wilson-Gordon and H. Friedman, Ultranarrow extraresonant antiholes in pump-probe spectroscopy induced by inelastic collisions, *Opt. Lett.* **14**, 390 (1989).
- [5] L. Margalit, M. Rosenbluh, and A. D. Wilson-Gordon, Degenerate two-level system in the presence of a transverse magnetic field, *Phys. Rev. A* **87**, 033808 (2013).
- [6] A. Lezama, S. Barreiro, A. Lipsich, and A. M. Akulshin, Coherent two-field spectroscopy of degenerate two-level systems, *Phys. Rev. A* **61**, 013801 (1999).
- [7] C. Goren, A. D. Wilson-Gordon, M. Rosenbluh, and H. Friedmann, Electromagnetically induced absorption due to transfer of coherence and to transfer of population, *Phys. Rev. A* **67**, 033807 (2003).
- [8] C. Goren, A. D. Wilson-Gordon, M. Rosenbluh, and H. Friedmann, Switching from positive to negative dispersion in transparent degenerate and near-degenerate systems, *Phys. Rev. A* **68**, 043818 (2003).
- [9] H. U. Rehman, M. Adnan, H.-R. Noh, and J. T. Kim, Spectral features of electromagnetically induced absorption in  $^{85}\text{Rb}$  atoms, *J. Phys. B: At. Mol. Opt. Phys.* **48**, 115502 (2015).
- [10] C. Goren, A. D. Wilson-Gordon, M. Rosenbluh, and H. Friedmann, Atomic four-level  $N$  systems, *Phys. Rev. A* **69**, 053818 (2004).
- [11] Y. Gu, Q. Sun, and Q. Gong, Quantum coherence in a degenerate two-level atomic ensemble for a transition  $F_g=3 \leftrightarrow F_e=4$ , *Phys. Rev. A* **67**, 063809 (2003).
- [12] A. Eilam and A. D. Wilson-Gordon, Temporal optical memory based on coherent population and two-photon coherence oscillations, *Phys. Rev. A* **98**, 013808 (2018).
- [13] H. U. Rehman, M. Q. Mohsin, H.-R. Noh, and J. T. Kim, Electromagnetically induced absorption due to transfer of coherence and coherence population oscillation for the  $F_g=3 \rightarrow F_e=4$  transition in  $^{85}\text{Rb}$  atoms, *Opt. Commun.* **381**, 127 (2016).
- [14] G. W. Choi and H.-R. Noh, Line shapes in sub-Doppler DAVLL in the  $^{87}\text{Rb}$ -D2 line, *Opt. Commun.* **367**, 312 (2016).
- [15] J. Fuchs, G. J. Duffy, W. J. Rowlands, A. Lezama, P. Hannaford, and A. M. Akulshin, Electromagnetically induced transparency and absorption due to optical and ground-state coherences in  $^6\text{Li}$ , *J. Phys. B: At. Mol. Opt. Phys.* **40**, 1117 (2007).
- [16] A. Lipsich, S. Barreiro, A. M. Akulshin, and A. Lezama, Absorption spectra of driven degenerate two-level atomic systems, *Phys. Rev. A* **61**, 053803 (2000).
- [17] A. M. Akulshin, S. Barreiro, and A. Lezama, Electromagnetically induced absorption and transparency due to resonant two-field excitation of quasidegenerate levels in Rb vapor, *Phys. Rev. A* **57**, 2996 (1998).
- [18] T. Zigdon, A. D. Wilson-Gordon, and H. Friedmann, Pump-probe spectroscopy in degenerate two-level atoms with arbitrarily strong fields, *Phys. Rev. A* **77**, 033836 (2008).
- [19] T. Zigdon, A. D. Wilson-Gordon, and H. Friedman, Absorption spectra for strong pump and probe in atomic beam of cesium atoms, *Phys. Rev. A* **80**, 033825 (2009).
- [20] H.-R. Noh and H. S. Moon, Calculated Hanle transmission and absorption spectra of the  $^{87}\text{Rb}D_1$  line with residual magnetic field for arbitrarily polarized light, *Phys. Rev. A* **82**, 033407 (2010).
- [21] H. Cheng, H.-M. Wang, S.-S. Zhang, P.-P. Xin, J. Luo, and H.-P. Liu, Electromagnetically induced transparency of  $^{87}\text{Rb}$  in a buffer gas cell with magnetic field, *J. Phys. B: At. Mol. Opt. Phys.* **50**, 095401 (2017).
- [22] A. Sargsyan, D. Sarkisyan, Y. Pashayan-Leroy, C. Leroy, S. Cartaleva, A. D. Wilson-Gordon, and M. Auzinsh, Electromagnetically induced transparency resonances inverted in magnetic field, *J. Exp. Theor. Phys.* **121**, 966 (2015).
- [23] R. Mirzoyan, A. Sargsyan, D. Sarkisyan, A. Wojciechowski, A. Stabrawa, and W. Gawlik, EIT resonance features in strong magnetic fields in rubidium atomic columns with length varying by 4 orders, *Opt. Spectrosc.* **120**, 864 (2016).
- [24] A. Sargsyan, D. Sarkisyan, L. Margalit, and A. D. Wilson-Gordon, Two strongly contrasting  $\Lambda$ -systems in the  $D_1$  line of  $^{87}\text{Rb}$  in a transverse magnetic field, *J. Exp. Theor. Phys.* **122**, 1002 (2016).
- [25] I. H. Subba and A. Tripathi, Observation of electromagnetically induced absorption in  $^{87}\text{Rb}D_2$  line in strong transverse magnetic field, *J. Phys. B: At. Mol. Opt. Phys.* **51**, 155001 (2018).
- [26] S. M. Iftiqar and V. Natarajan, Line narrowing of electromagnetically induced transparency in Rb with a longitudinal magnetic field, *Phys. Rev. A* **79**, 013808 (2009).
- [27] L. Margalit, M. Rosenbluh, and A. D. Wilson-Gordon, Coherent-population-trapping transients induced by a modulated transverse magnetic field, *Phys. Rev. A* **88**, 023827 (2013).
- [28] R. W. Boyd, *Nonlinear Optics* (Academic Press, Boston, 1992).
- [29] DLPro, Toptica Inc.
- [30] M. Fleischhauer and M. D. Lukin, Dark-State Polaritons in Electromagnetically Induced Transparency, *Phys. Rev. Lett.* **84**, 5094 (2000).